Quasiclassical Trajectory Study of Energy Transfer and Collision-Induced Dissociation in Hyperthermal Ar + CH_4 and Ar + CF_4 Collisions

Diego Troya*

Department of Chemistry, Virginia Tech, Davidson Hall 107, Blacksburg, Virginia 24061-0212

Received: April 7, 2005; In Final Form: May 12, 2005

We present a study of energy transfer in collisions of Ar with methane and perfluoromethane at hyperthermal energies (E_{coll} = 4−10 eV). Quasiclassical trajectory calculations of Ar + CX_4 (X = H, F) collisions indicate that energy transfer from reagents' translation to internal modes of the alkane molecule is greatly enhanced by fluorination. The reasons for the enhancement of energy transfer upon fluorination are shown to emerge from a decrease in the hydrocarbon vibrational frequencies of the CX_4 molecule with increasing the mass of the X atom, and to an increase of the steepness of the Ar−CX_4 intermolecular potential. At high collision energies, we find that the cross section of Ar + CF_4 collisions in which the amount of energy transfer is larger than needed to break a C−F bond is at least 1 order of magnitude larger than the cross sections of Ar + CH_4 collisions producing CH_4 with energy above the dissociation limit. In addition, collision-induced dissociation is detected in short time scales in the case of the fluorinated species at E_{coll} = 10 eV. These results suggest that the cross section for degradation of fluorinated hydrocarbon polymers under the action of nonreactive hyperthermal gas-phase species might be significantly larger than that of hydrogenated hydrocarbon polymers. We also illustrate a practical way to derive intramolecular potential energy surfaces for bond-breaking collisions by improving semiempirical Hamiltonians based on grids of high-quality ab initio calculations.

Introduction

Understanding how energy flows between modes during the course of a molecular collision has long been a driving force for collisional energy transfer studies. In early efforts, collisional energy transfer was studied as a key step in the determination of unimolecular reaction rates, and significant activity was directed at characterizing the mechanisms whereby highly internally excited molecules lose energy to a bath of nonreactive species through collisional energy transfer.[1−4] New interest in the field of collisional energy transfer is emerging due to the presence of collisions of hyperthermal species with gas-phase molecules and surfaces in a variety of environments.

A paradigmatic example of an environment in which hyperthermal collisions are important is low-Earth orbit (LEO). Spacecraft operating in LEO collide with the natural gaseous species of the LEO atmosphere at ∼8 km/s. Such hyperthermal collisions result in degradation of the polymers used to coat spacecraft.[5,6] The most abundant species of the LEO region (100−700 km altitude) is atomic oxygen in the ground state ($O(^3P)$). Thus, vigorous activity from both experimental[7,8] and theoretical[9,10] perspectives has been aimed at characterizing the reactions of $O(^3P)$ with hydrocarbons at hyperthermal energies as a model to derive fundamental understanding of the mechanisms whereby hydrocarbon polymers degrade in LEO.

Although atomic oxygen is the most abundant species in LEO, the number densities of other gaseous neutral species are also significant, particularly at low altitudes. For instance, at 150 km altitude, the number density of N_2 is comparable to that of $O(^3P)$, and the number density of Ar atoms is only about 2 orders of magnitude smaller. Both N_2 and Ar are closed-shell species, and until recently, the possible deleterious effects of these species on spacecraft polymers had been ignored. However, Ar and N_2 are roughly twice heavier than atomic oxygen, which gives rise to relative collision energies with spacecraft polymers roughly twice larger than in the case of atomic oxygen. (E_{coll} ≈ 8 eV (11 eV) for N_2 (Ar) collisions with the polymer surfaces perpendicular to the direction of travel of the spacecraft.) The collision energies associated with these hyperthermal encounters are well in excess of the dissociation energies of many chemical bonds in the polymers. Therefore, large collisional energy transfer from initial translation to molecular motions could result in polymer degradation by collision-induced dissociation.

Recent experimental work by the Minton group has shown that hyperthermal collisions of Ar and N_2 with hydrocarbon polymers result in the degradation of the polymers.[11,12] In those experiments, hyperthermal beams of Ar and N/N_2 were directed at oxidized polymer surfaces. The detection of volatile CO and CO_2 species upon collision of fast Ar and N_2 on the oxidized polymer clearly indicates that the energy transfer from the hyperthermal Ar and N_2 species to the polymers is large enough to produce breakage of chemical bonds in the polymer surface. More recently, the same group measured the extent of collisional energy transfer in collisions of hyperthermal Ar with C_2H_6 (E_{coll} ≤ 5 eV).[13] The results indicated that some collisions can produce highly vibrationally excited ethane.

In this paper, we present a theoretical study of collisional energy transfer and collision-induced dissociation in hyperthermal collisions between Ar and CX_4 (X = H, F). Our goal is to give an initial step toward the characterization at the theoretical level of the role of hyperthermal collisions between closed-shell species and polymeric hydrocarbons in polymer degradation. Comparison between Ar + CH_4 and CF_4 collisions is motivated by experimental measurements of the erosion rates of hydrogenated and fluorinated hydrocarbon polymers in the LEO environment. On-orbit measurements indicate that fluori-

* E-mail: troya@vt.edu.

10.1021/jp051808e CCC: $30.25
Published on Web 06/10/2005

nated polymers, such as TEFLON, erode somewhat more slowly than analogous hydrogenated polymers (such as polyethylene) in LEO.[14] Recent theoretical studies indicate that the reactivity of atomic oxygen with fluorinated hydrocarbons is marginal under LEO conditions.[15] According to these calculations, if $O(^3P)$ was the only species accountable for damage, fluorinated polymers should erode at a much smaller rate than they actually do in the LEO environment. It is therefore plausible that sources of erosion other than atomic oxygen play a major role in the degradation of fluorinated polymers. UV radiation has been identified as one source of damage.[16,17] However, the contribution of hyperthermal collisions with N_2 or Ar is currently unknown. The work presented here is aimed at clarifying the potential importance of collision-induced dissociation in hydrogenated and fluorinated hydrocarbons produced by hyperthermal impacts of nonreactive species, such as Ar.

Another goal of this work is to advance our knowledge of a practical and relatively unexplored way to derive potential energy surfaces for reaction dynamics calculations. The strategy for constructing such potential energy surfaces is based on the development of accurate quantum-mechanical semiempirical Hamiltonians that permit direct-dynamics calculations. The method is general and can be applied to a variety of chemical reactions, including collision-induced dissociation.

Potential Energy Surface

Predictive characterization of collisional energy transfer in collisions of Ar with hydrocarbon species requires use of an accurate potential energy surface describing the interactions between Ar and the hydrocarbons (intermolecular potential), and within the hydrocarbons (intramolecular potential). In this section, we separately describe the derivation of the intermolecular and intramolecular potential energy surfaces employed in our dynamics studies of collisions of Ar with CH_4 and CF_4.

A. Intermolecular Potential. The shape of the intermolecular potential between Ar and CH_4 is characterized by a shallow well at long Ar−CH_4 distances, and a repulsive wall at short distances. The relatively simple profile of this potential energy surface allows for derivation of analytical functions that reproduce ab initio calculations. The most accurate intermolecular potential for Ar−CH_4 collisions available to date was derived by Hase and co-workers by fitting pairwise generalized exponential functions to QCISD(T)/6-311++G** ab initio calculations.[18] The analytical intermolecular potential energy surface derived in that work accurately describes the electronic structure calculations up to energies of about 5 eV. In this work, we are interested in collision energies in the 4−10 eV range. Therefore, using a similar approach, we have developed a new analytical function that reproduces ab initio calculations covering the regions of the potential energy surface explored in the hyperthermal collisions studied here.

Our pairwise analytical function for the Ar−CH_4 intermolecular potential energy term has the form:

$$V_{ij} = a \exp(-br_{ij}) + c/r_{ij}^{\,d} \qquad (1)$$

where i = Ar and j = C or H, and r_{ij} is the internuclear distance between Ar and C or H. The *a*, *b*, *c*, and *d* adjustable parameters have been derived based on CCSD(T)/cc-pVTZ calculations of the energy of three approaches of Ar to the CH_4 molecule: collinear to a C−H bond (C_{3v} symmetry), perpendicular to one of the faces of the CH_4 tetrahedron (C_{3v} symmetry), and bisecting a H−C−H angle (C_{2v} symmetry). Overall, we have calculated 178 points at the CCSD(T)/cc-pVTZ level to obtain a good coverage of the intermolecular potential energy surface. Figure 1a shows the ab initio data points compared with the best fit provided by the analytical function of eq 1. Both sets of energies are in excellent agreement throughout the energy regime relevant to our dynamics calculations. The parameters of the analytical function are reported in Table 1.

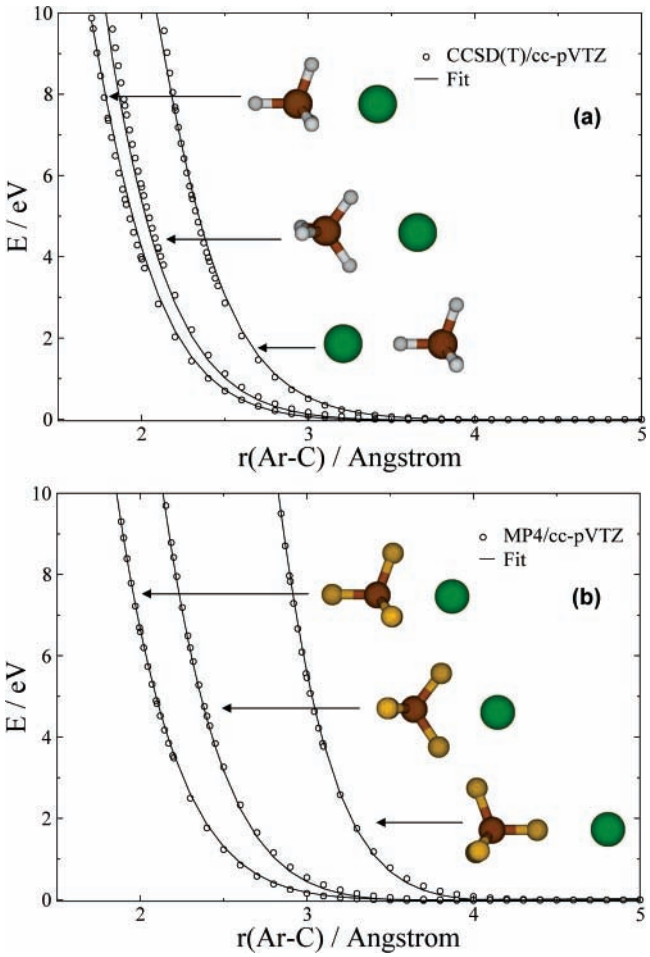

Figure 1. Comparison of analytical and ab initio intermolecular potential energy in three approaches of Ar to CX_4: (a) Ar−CH_4 and (b) Ar−CF_4.

TABLE 1: Parameters of the Pair-Wise Generalized Exponential Function (see Eq 1) Describing the Ar−CX_4 (X = H, F) Intermolecular Potential[a]

	a_{ij}	b_{ij}	c_{ij}	d_{ij}
Ar−CH_4				
i = Ar, j = H	6908.0024	3.19515	−105.2819	5.228089
i = Ar, j = C	165557.2031	3.54001	−13103.1045	7.452095
Ar−CF_4				
i = Ar, j = F	99140.4531	3.63198	−2396.7034	6.214203
i = Ar, j = C	4163.6846	2.27087	−921.3834	7.809786

[a] Units are such that if r_{ij} is in Å, V_{ij} is in kcal/mol.

We have adopted an analogous strategy to derive an analytical intermolecular potential energy function for collisions of Ar with CF_4. However, calculation of over 100 points at the CCSD(T) level with the cc-pVTZ basis set becomes computationally expensive for this system due to the abrupt increase in CPU time of CCSD(T) methods with an increasing number of electrons. To alleviate the computational expense without drastically compromising the accuracy of the calculations, we have restricted the level of electronic correlation to fourth-order Møller−Plesset perturbation theory (MP4, including single, double, triple, and quadruple excitations). Thus, MP4/cc-pVTZ

calculations are used to describe the potential energy of the three approaches of Ar to the CF_4 tetrahedral molecule mentioned above for CH_4 (i.e., collinear to a C−F bond, perpendicular to a tetrahedral face, and bisecting a F−C−F angle). Overall, 130 ab initio points were included in the fit of the analytical function shown in eq 1 for the Ar−CF_4 intermolecular potential. Comparisons between the ab initio data points and the analytical function are shown in Figure 1b, and excellent agreement between the ab initio and the fitted values can be noted. The adjustable parameters of the analytical function are reported in Table 1.

We have verified the legitimacy of MP4 calculations by performing CCSD(T) calculations on selected points of the Ar−CF_4 intermolecular potential energy surface. MP4 calculations provide good estimates of CCSD(T) energies in all cases. For instance, for the approach of Ar to CF_4 along one of the F−C−F bisectors, the MP4/cc-pVTZ energy at an Ar−C distance of 2.153 Å is 9.693 eV (referred to separated reagents). The energy at the CCSD(T)/cc-pVTZ level is 9.737 eV. These calculations differ by about 1 kcal/mol, which is well below 1% of the total potential energy. For the approach collinear to one of the C−F bonds, the MP4/cc-pVTZ energy is 9.499 eV at an Ar−C distance of 2.845 Å. The CCSD(T)/cc-pVTZ value is 9.539 eV, ∼0.9 kcal/mol larger than the MP4 value. Finally, for the approach of Ar perpendicular to one of the CF_4 tetrahedron faces, the MP4/cc-pVTZ energy at an Ar−C distance of 1.885 Å is 9.302 eV. The corresponding CCSD(T)/cc-pVTZ energy is 9.336 eV, ∼0.8 kcal/mol larger than the less accurate result. These sample calculations demonstrate that our choice of the MP4 method to explore the repulsive wall of the Ar−CF_4 potential energy surface introduces only a marginal error in the intermolecular potential energy surface.

It should be noted that although the analytical intermolecular terms derived here are a good representation of the repulsive wall, they are not so accurate for the shallow van der Waals well region occurring at longer Ar−CX_4 distances. For instance, the well of the analytical function is 2.5 times deeper than estimated with ab initio calculations in both Ar + CH_4 and Ar + CF_4. Notwithstanding, the errors in this region of the intermolecular potential energy surface are not important in our study because the collision energies of the trajectories are at least 2 orders of magnitude larger than the van der Waals well depth.

B. Intramolecular Potential. The main challenge in performing theoretical studies of noble-gas/molecule encounters that lead to collision-induced dissociation in the molecule is tied to the development of an accurate intramolecular potential. The intramolecular potential energy surface describes the interactions within the molecule and must accurately describe bond-breakage processes if collision-induced dissociation is possible. In the case of methane, several analytical potential energy surfaces have been published in studies of $CH_4 \rightarrow CH_3 + H$[19−21] and Ar + CH_4.[22,23] Although such intramolecular potential energy surfaces could have been readily employed in our study of hyperthermal Ar + CH_4 collisions, we would still have been faced with the necessity of deriving an intramolecular surface for CF_4. Thereby, we have preferred to derive new potential energy surfaces for both CH_4 and CF_4. The surfaces are developed by using analogous strategies so that legitimate comparisons between the dynamics of Ar + CH_4 and CF_4 collisions can be established.

Instead of deriving an analytical potential energy surface based on quantum-mechanical calculations and using it in subsequent trajectory calculations, our approach is to evaluate the potential energy and energy gradients of the CH_4 and CF_4 molecules directly from quantum-mechanical calculations while the trajectories are evolving. This technique is best known as "direct-dynamics".[24] The main advantage of this procedure is that the process of deriving an analytical potential energy surface is avoided altogether. The disadvantage of calculating the intramolecular potential energy directly with quantum-mechanical calculations is in the large computational overhead that this approach poses. For trajectory studies such as the one presented here, the total number of required gradient calculations is in the 10^6-10^8 range. Such a large number of gradient evaluations prohibits use of first-principles methods.

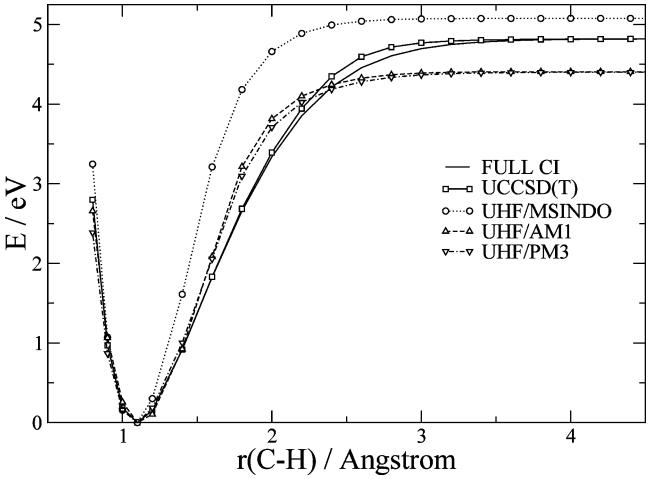

Figure 2. Calculated C−H bond dissociation energy curves in CH_4. The geometry of the CH_3 moiety is held fixed in the calculations (C−H distance = 1.089 Å, tetrahedral angles). The first-principles data correspond to calculations with the 6-31G* basis set. The FULL-CI data are taken from ref 26.

To make direct-dynamics calculations viable, we resort to using semiempirical methods. Quantum-mechanical semiempirical Hamiltonians reduce the computational effort associated with first-principles electronic-structure calculations by including empirical parameters in (mainly) two-center integrals.[25] These parameters are typically derived based on high-accuracy ab initio calculations or experiments on a limited database of chemical reactions. Therefore, although semiempirical Hamiltonians exhibit an excellent accuracy/computing-time ratio for the reactions included in the database, the accuracy of these methods is not general for every chemical reaction in all of the regions of the potential energy surface. An example of the limitations of semiempirical methods is given by the dissociation energy curves of a C−H bond in methane displayed in Figure 2. The FULL-CI calculations of ref 26 are compared with UCCSD(T) data, and with the estimates of the MSINDO,[27,28] AM1,[29] and PM3[30] semiempirical Hamiltonians. The ab initio calculations have been performed with the Gaussian03 code,[31] and the AM1 and PM3 calculations have been carried out with the GAMESS suite of programs.[32] Figure 2 shows that whereas AM1 and PM3 underestimate the C−H bond dissociation energy in methane, the MSINDO semiempirical Hamiltonian overestimates it.

Dynamics calculations of hyperthermal Ar + CH_4 collisions with the MSINDO, AM1, or PM3 semiempirical Hamiltonians would likely result in inaccurate estimates of the extent of collisional energy transfer, and particularly collision-induced dissociation. However, as mentioned above, use of accurate first-principle methods in extensive direct-dynamics calculations including thousands of trajectories is impossible at this time. An emerging approach to deal with the accuracy issues of semiempirical Hamiltonians is to optimize the set of empirical

parameters so that the Hamiltonian reproduces highly accurate ab initio calculations only for the reaction under consideration.[33,34] The semiempirical Hamiltonian derived in this way is termed the specific-reaction-parameters (SRP) Hamiltonian.[35] In this work, we explore the viability of developing SRP Hamiltonians to treat energy transfer and collision-induced dissociation in Ar + CH_4, CF_4 collisions. It should be noted that this approach to construct potential energy surfaces is general and can be straightforwardly extended to collisions involving species with, in principle, an arbitrary number of degrees of freedom.

We have derived SRP-MSINDO Hamiltonians for the CH_4 and CF_4 molecules by optimizing the parameters of the MSINDO Hamiltonian for both of these molecules so that semiempirical calculations reproduce high-quality ab initio data. We use a home-designed nonlinear least-squares procedure based on the minpack libraries[36] to optimize the set of semiempirical parameters so that the differences between semiempirical and ab initio energies are minimum. In the case of CH_4, we initially calculated 99 points of the methane C−H dissociation energy curve at the UCCSD(T)/cc-pVTZ level as a database for optimization of the MSINDO parameters. During the parameter optimization, we discovered that one can get semiempirical calculations to perfectly match the ab initio C−H dissociation energy curve at the expense of introducing flaws in other regions of the CH_4 surface. To avoid spurious behavior in regions of the potential energy surface removed from the C−H dissociation pathway, but accessible in hyperthermal collisions, we have included a total of 399 UCCSD(T)/cc-pVTZ data points in the optimization of the MSINDO semiempirical Hamiltonian. As mentioned above, 99 of these high-accuracy points correspond to the C−H dissociation energy curve. Additional points were calculated to describe the H−C−H bending energy curve (56 points) up to ∼4 eV, the symmetric stretching mode of methane (102 points) up to ∼6 eV, and the CH_2 + H_2 asymptote (42 points). These points describe the regions of the potential energy surface explored in the extreme case that the energy transferred from the striking Ar atom is channeled predominantly to one vibration mode. However, in real collisions, many vibration modes can be excited.

To take into account simultaneous excitation of all of the vibration modes in our grid of high-accuracy ab initio calculations, we have calculated 100 points corresponding to highly excited configurations of methane. The points are obtained from a "root trajectory" of methane in which all of the normal modes are vibrationally excited. The root trajectory is initiated giving 2.5 quanta of excitation to each normal mode (∼6 eV of total excitation) and is integrated with GAMESS at the UMP2/aug-cc-pVDZ level during 1 ps. The instantaneous geometry of the methane molecule in such a root trajectory is extracted every 10 fs, and the energy is refined at the UCCSD(T)/cc-pVTZ level. The potential energies explored during the root trajectory range from 1 to 5 eV. Figure 3 shows the energies of the 100 points at the UCCSD(T)/cc-pVTZ level, compared with the estimates of the original MSINDO Hamiltonian and the SRP-MSINDO Hamiltonian derived here. The figure shows that the SRP-MSINDO Hamiltonian is remarkably more accurate than the original Hamiltonian. Likely, the inclusion of these 100 points in the derivation of SRP parameters not only helps improve the global accuracy of the SRP MSINDO semiempirical Hamiltonian, but also reduces the possibility of spurious behavior of the Hamiltonian in regions not included in the optimization.

Figure 4 shows a comparison of the C−H dissociation energy curve at the UCCSD(T)/cc-pVTZ level (using UMP2/cc-pVTZ-optimized geometries), with the estimates of the original and SRP-MSINDO Hamiltonians. The dissociation energy curve of the standard AM1 Hamiltonian is included for the sake of performance comparison. The corresponding dissociation energies are reported in Table 2 in comparison with experiments. The SRP-MSINDO Hamiltonian provides a good description of the UCCSD(T) data, particularly with regard to the repulsive wall, the minimum-energy region, and the asymptote. The agreement is not so excellent in the region of the curve where the energy bends over toward the asymptote. This region of

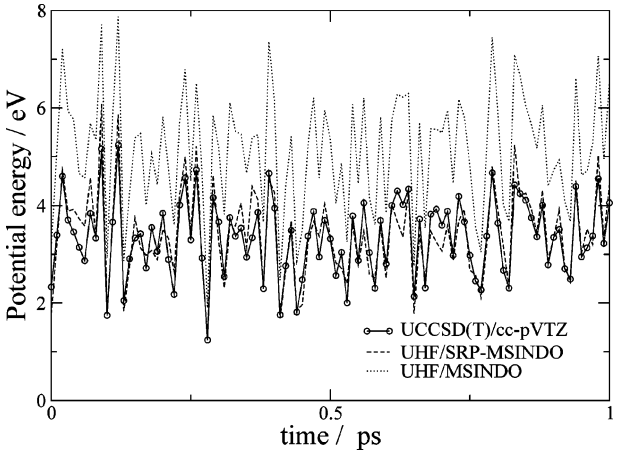

Figure 3. Comparison of UCCSD(T)/cc-pVTZ data points with SRP-MSINDO and MSINDO estimates for highly excited configurations of CH_4. The points correspond to single-point calculations of instantaneous geometries of a methane root trajectory initiated with 2.5 quanta of vibrational excitation in each normal mode and integrated for 1 ps.

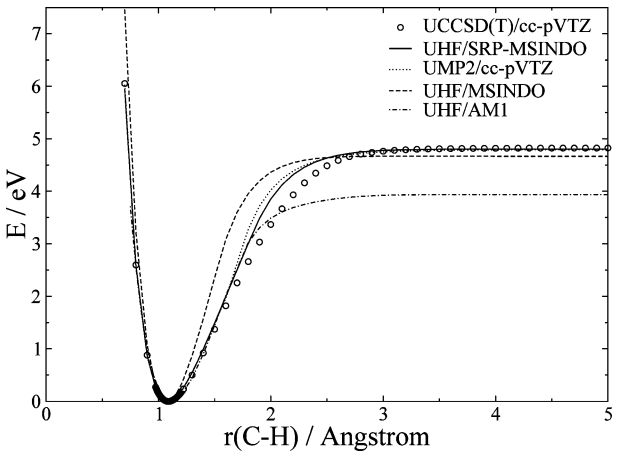

Figure 4. Calculated C−H bond dissociation energy curves in CH_4. The geometry of the CH_3 moiety is optimized in the calculations. UCCSD(T)/cc-pVTZ calculations are performed with geometries optimized at the UMP2/cc-pVTZ level.

TABLE 2: C−X Bond Dissociation Energies in the CX_4 (X = H, F) Molecules[a]

	CH_4	CF_4
MSINDO	4.667	5.116
AM1	3.939	4.345
B3LYP/cc-pVTZ	4.828	5.508
SRP-MSINDO	4.802	5.736
UCCSD(T)/cc-pVTZ	4.825	5.653
exptl	4.861[b]	5.698 ± 0.043[c]

[a] Energies are in eV. Values are not corrected with zero-point energies. [b] Obtained from the experimental heats of formation at 0 K,[42] and using experimental zero-point energies for CH_4 and CH_3.[43] [c] Obtained from the experimental heats of formation at 0 K,[44] and using experimental zero-point energies for CF_4[45] and CF_3.[46]

TABLE 3: Original MSINDO Parameters for the H, C, and F Atoms and SRP-MSINDO Parameters for the Ar + CH_4 → Ar + CH_3 + H and Ar + CF_4 → Ar + CF_3 + F Processes[a]

	Ar + CH_4				Ar + CF_4			
	H		C		F		C	
	original	SRP	original	SRP	original	SRP	original	SRP
				orbital exponents				
ξ_s^U	1.0060	0.6663	1.6266	0.9590	2.3408	2.1107	1.6266	1.0697
ξ_p^U			1.5572	1.3320	2.2465	2.0046	1.5572	1.1821
ξ_s	1.1576	0.9862	1.7874	3.3876	2.4974	2.7320	1.7874	7.0992
ξ_p			1.6770	1.3789	2.3510	2.2119	1.6770	1.0891
				valence-state ionization potentials				
I_s	0.5000	0.3244	0.8195	0.4648	2.0238	3.4591	0.8195	0.7383
I_p					0.6868	0.9208	0.3824	0.7242
				resonance integral parameters				
K_σ	0.1449	0.1226	0.0867	0.0516	0.1769	0.0783	0.0867	0.0767
K_π					0.0127	0.0154	0.0478	0.0065
k_1	0.3856	0.6389	0.4936	0.4129				
k_2	0.5038	0.2166			0.1059	0.1212	0.6776	2.3954

[a] For of a detailed explanation of the parameters see ref 27.

the potential energy surface seems particularly difficult to describe, as shown by the UMP2/cc-pVTZ points included in the figure. Interestingly, UMP2/cc-pVTZ calculations compare well with the SRP-MSINDO data throughout the range of C−H distances explored in our calculations, but SRP-MSINDO shows better performance in the region of slight disagreement with UCCSD(T) values. The original and improved SRP-MSINDO parameters for the C and H atoms are shown in Table 3.

It should be noted that in the fitting, the semiempirical energies are calculated by using the same geometries as in the ab initio points for the symmetric stretch, the $CH_2 + H_2$ asymptote, and the root trajectory. The geometries of the symmetric stretch are obtained by scanning the C−H coordinate while keeping the tetrahedral symmetry of the molecule. The geometries of the points of the $CH_2 + H_2$ asymptote and root trajectory are calculated at the UMP2/AUG-cc-pVDZ level. In the case of the C−H dissociation energy curve, we fix one of the C−H distances and optimize the rest of coordinates in both the ab initio (at the UMP2/cc-pVTZ level) and semiempirical calculations. For the bending data points, we fix the bending angle in the ab initio calculations and optimize the rest of coordinates at the UMP2/cc-pVTZ level. In the semiempirical calculations, we fix the three atoms that define the bending angle at the ab initio-optimized values, and optimize the rest of the coordinates.

A similar approach has been adopted to derive a SRP-MSINDO Hamiltonian for the CF_4 molecule. Unfortunately, we cannot afford calculation of hundreds of points at the UCCSD-(T)/cc-pVTZ level for this system, and therefore we need to use other methods. Table 2 shows that UB3LYP/cc-pVTZ calculations are in excellent agreement with the UCCSD(T) and experimental C−H dissociation energies in methane. Additional calculations (not shown) reveal that the agreement with UCCSD-(T) data occurs throughout the calculated interval of C−H distances. Table 2 also shows that the agreement between UB3LYP/cc-pVTZ calculations and UCCSD(T)/cc-pVTZ calculations for the C−F dissociation energy in CF_4 is also good, but not as excellent as in the case of CH_4. Both sets of calculations compare well with experiments. Although the UCCSD(T) value is within the experimental uncertainty, as mentioned before, it is prohibitive for us to use this method for many points. The computational demand of the UB3LYP method is much more relaxed, but the C−F bond dissociation energy value is very close to UCCSD(T) estimates. Thus, we have used UB3LYP/cc-pVTZ calculations to generate a grid of points for improvement of the MSINDO semiempirical Hamiltonian. To improve the accuracy of the energies calculated at the UB3LYP/cc-pVTZ level, we linearly scale these energies so that the scaled UB3LYP/cc-pVTZ C−F dissociation energy matches the UCCSD(T)/cc-pVTZ value. The scaling factor is $E_{(\text{scaled})\text{B3LYP}} = E_{\text{B3LYP}}(5.654/5.508)$, where E_{B3LYP} and $E_{(\text{scaled})\text{B3LYP}}$ are the energies of the CF_4 molecule referred to the energy of the equilibrium geometry.

The grid of scaled UB3LYP energies consists of 292 points. Seventy eight of these points are for the C−F dissociation energy curve, 47 points belong to the F−C−F bending energy curve, 51 points are for the symmetric stretch, and 16 are for the $CF_2 + F_2$ asymptote (which is closed at the energies of our dynamics calculations). The remaining 100 points have been calculated at the UB3LYP/cc-pVTZ level from a "root trajectory" and started giving 5.5 quanta of vibrational excitation to each normal mode of CF_4 (∼5 eV of total excitation). The grid of 292 points is used to optimize the parameters of the MSINDO Hamiltonian with use of the same nonlinear least-squares procedure mentioned before. The parameters of the C and F atoms that minimize the deviation between the scaled UB3LYP/cc-pVTZ data and the semiempirical values are shown in Table 3.

Regarding the geometries used in the parameter fitting for CF_4, we have used an approach similar to that for CH_4. The geometries of the points of the symmetric stretch are identical in the ab initio and semiempirical calculations and are obtained by scanning the C−F coordinate in the case of the symmetric stretch, fixing the C−F distance to 1.33 Å, and scanning the F−C−F angle in C_{3v} symmetry for the umbrella motion. The semiempirical calculations of the $CF_2 + F_2$ asymptote and root trajectory are carried out with geometries obtained from UB3LYP/6-31+G* and UB3LYP/3-21G* calculations, respectively. Note that although in obtaining the geometries of these data points we have used relatively small basis sets, the energies are refined at the UB3LYP/cc-pVTZ level before the fitting. As with CH_4, the geometries for the C−F dissociation energy curves are obtained by fixing the C−F distance that is being varied, and letting the rest of the coordinates in the first-principles (at the UB3LYP/cc-pVTZ level) and semiempirical calculations be optimized. For the UB3LYP calculation of bending points, we fix one of the molecular angles and relax the rest of the coordinates with the cc-pVTZ basis set. In the semiempirical calculations of the bending points, we fix the three atoms that define the bending angle at the UB3LYP-optimized values and optimize the rest of the coordinates.

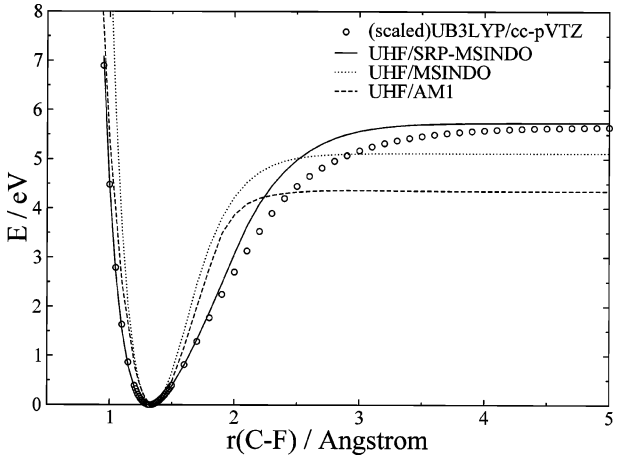

Figure 5. Calculated C−F bond dissociation energy curves in CF_4. The geometry of the CF_3 moiety is optimized in the calculations. (scaled)B3LYP/cc-pVTZ corresponds to B3LYP/cc-pVTZ-optimized data points which energies have been scaled so that the C−F dissociation energy matches UCCSD(T)/cc-pVTZ results.

Figure 5 shows the comparison between the C−F dissociation energy curves obtained with the MSINDO, AM1, and SRP-MSINDO semiempirical Hamiltonians and the (scaled)UB3LYP/cc-pVTZ data. SRP-MSINDO correctly describes the dissociation energy, which is an improvement over the original MSINDO Hamiltonian and the AM1 Hamiltonian. The parameter optimization also improves the agreement with more accurate calculations in regions other than the asymptote, but much as we have indicated in the case of CH_4, there is a slight disagreement in the region where the curve bends over toward the asymptote. Likely, the functional form of the MSINDO semiempirical Hamiltonian is not flexible enough to obtain quantitative descriptions in this region of the dissociation energy curve for both CH_4 and CF_4 without introducing spurious behavior in other regions of the potential energy surface. The calculated dissociation energies are compared with experiments in Table 2.

To verify the adequacy of our scaling factor for the B3LYP energies in regions other than the $F-CF_3$ dissociation energy curve, we have carried out CCSD(T)/cc-pVTZ calculations of the three points of highest energy of the CF_4 root trajectory. The CCSD(T) energies of these points are 5.955, 5.021, and 4.943 eV. The B3LYP/cc-pVTZ results are 5.566, 4.731, and 4.629 eV, respectively. These energies become closer to the CCSD(T) estimates when we apply the $E_{(\text{scaled})\text{B3LYP}} = E_{\text{B3LYP}}$-(5.654/5.508) scaling factor (5.712, 4.856, and 4.751 eV). Thus we see that although the agreement between the scaled (B3LYP) and CCSD(T) energies is not quantitative in regions of the potential energy surface other than the dissociation energy curve, the scaling factor helps decrease the overall difference between B3LYP and CCSD(T) data.

Using the inter- and intramolecular potential energy surfaces described above, we have performed quasiclassical trajectory calculations of $Ar + CH_4$ and CF_4 collisions at hyperthermal energies with the goal of examining the extent of energy transfer and collision-induced dissociation in these systems.

Dynamics Study

A. Computational Details. We use the quasiclassical trajectory method to study the dynamics of $Ar + CH_4$ and CF_4 collisions at hyperthermal energies. Batches of 10 000 and 5 000 trajectories are integrated at 4, 5, 6, 7, 8, 9, and 10 eV collision energies for $Ar + CH_4$ and $Ar + CF_4$, respectively. The lowest collision energy of this study (4 eV) corresponds to a collision velocity of 8.2 km/s in the $Ar + CH_4$ center of mass and 5.3 km/s in the $Ar + CF_4$ center of mass. The largest collision energy of this study (10 eV) corresponds to 13.0 km/s in the $Ar + CH_4$ center of mass and 8.4 km/s in the $Ar + CF_4$ center of mass. The trajectories are started at an initial separation between the Ar atom and the center of mass of the CX_4 (X = H, F) molecule of 8 Å. We stop the trajectories when one of the Ar−X or Ar−C distances reaches 10 Å. This separation is large enough that the interaction between the noble gas and the molecule is negligible. For $Ar + CH_4$ collisions, the equations of motion are solved every 10 au with use of our home-designed trajectory propagation code, which employs a fifth-order predictor, sixth-order corrector integrator. The integration step is small enough that the total energy of the inelastic collisions is conserved to better than 10^{-4} hartree. In $Ar + CF_4$ collisions, the absence of fast motions associated with hydrogen atoms enables us to use a larger time integration step (15 au), without jeopardizing total energy conservation.

Potential energy and energy gradients are calculated at each integration step by using the potential energy method described before. The self-consistent-field (SCF) cutoff in the UHF/SRP-MSINDO calculations of the CH_4 and CF_4 intramolecular potential energy is set to 10^{-6} au. The major computational bottleneck of this study is associated with the fact that we cannot use the optimized molecular orbitals of a previous integration step as an initial guess for the SCF calculation of a given step. The correct calculation of the energy of a dissociating singlet species requires unrestricted wave functions in which the α and β orbital spaces are inequivalent. Therefore fresh, broken-symmetry wave functions need to be used at each integration step to ensure convergence to the correct limit while the trajectory is evolving.

We use the VENUS code of Hase et al.[37] to prepare the initial conditions of the CX_4 molecules. Fixed normal-mode energies are assigned to the molecules according to a thermal sampling of vibrational quantum numbers at 300 K. $RT/2$ ($T = 300$ K) rotational energy is given about each axis of the tetrahedral molecules.

The focus of this work is on collisions that give rise to large amounts of translational → internal (T → INT′) energy transfer. These collisions occur at small impact parameters. To obtain good statistics of these collisions, we choose a maximum impact parameter of $b_{\max} = 7.56$ au (4.0 Å) in our sampling for both $Ar + CH_4$ and $Ar + CF_4$ collisions. The range of impact parameters sampled emphasizes trajectories in which substantial energy transfer is produced, although it does not cover all of the inelastically scattered trajectories. Our tests indicate that the chosen $b_{\max}$ is large enough to cover trajectories that have deflection angles of at least 5°, and therefore, the results we present correspond to trajectories with scattering angles in the 5−180° range for both $Ar + CH_4$ and $Ar + CF_4$.

Although we report product rotational and vibrational energies, it should be noted that substantial Coriolis coupling is expected in the product molecule. This coupling between rotational and vibrational modes will make the product rotational and vibrational energy fluctuate in time. Thus, although the internal energy of the CX_4 fragment will be constant after the collision, the rotational and vibrational energies will change.

B. Collisional Energy Transfer. Figure 6 shows the product relative translational energy distributions in $Ar + CX_4$ (X = H, F) trajectories at collision energies in the 4−9 eV range. It can clearly be seen that Ar recoils more slowly from collisions with CF_4 than from collisions with CH_4. The peak of the

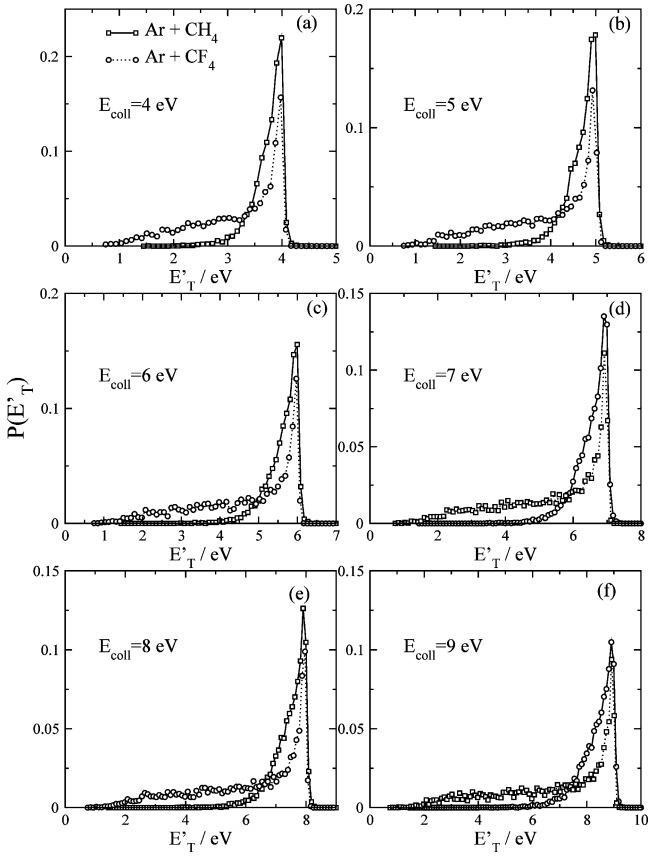

Figure 6. Calculated product translational energy distributions in hyperthermal Ar + CX_4 (X = H, F) collisions: (a) E_{coll} = 4 eV; (b) E_{coll} = 5 eV; (c) E_{coll} = 6 eV; (d) E_{coll} = 7 eV; (e) E_{coll} = 8 eV; (f) E_{coll} = 9 eV.

distributions occurs at 95−98% of the initial collision energy, indicating that most of the trajectories transfer very little energy from initial collision to molecular modes during the course of the collision in the range of selected impact parameters. Interestingly, the product translational distributions of Ar + CF_4 collisions are much broader than those of Ar + CH_4 collisions, indicating enhanced energy transfer upon fluorination of the alkane. We note that in a small fraction of the collisions, the final Ar translational energy is larger than the initial collision energy. In these collisions, the CX_4 molecule transfers energy from its internal modes to products' relative translation, ending up with internal energy below its zero-point in most cases. This is a well-known deficiency of classical-dynamics methods, and has been identified before in studies of Ar + C_2H_6 collisions.[13]

Figure 7 shows the evolution with collision energy of the average fractions of energy in products' translation, vibration, and rotation in Ar + CX_4 (X = H, F) collisions. Most of the collisions in which Ar scatters in the 5−180° angular interval do not transfer a significant fraction of the collision energy. Thus, the largest fraction of energy in products is in relative translational energy. The average fraction of product translation does not change with collision energy in Ar + CH_4, and it decreases very mildly with increasing collision energy in Ar + CF_4. Figure 7 shows that collisional energy transfer to CF_4 is more efficient than that to CH_4. The average fraction of internal energy of the CX_4 product is 3.7 times larger in Ar + CF_4 than in Ar + CH_4 at E_{coll} = 4.0 eV, and 3.9 times larger at E_{coll} = 10.0 eV. At the lower collision energies of this study, most of the energy transferred to the CH_4 molecule in Ar + CH_4 collisions goes into CH_4 rotation. The average fraction of rotational energy in CH_4 decreases slightly with collision energy

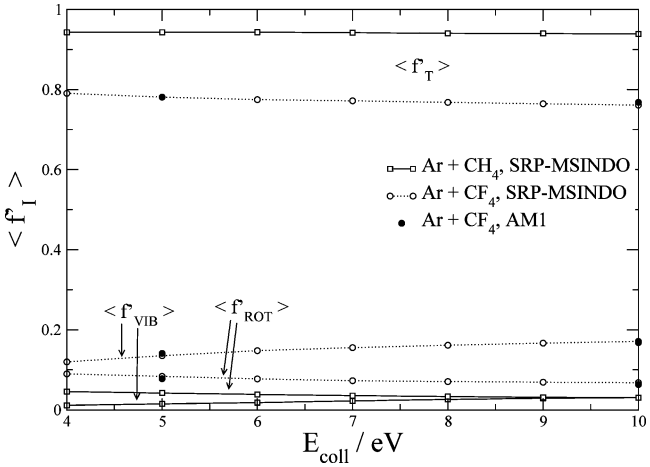

Figure 7. Average fractions of energy in products in Ar + CX_4 (X = H, F) collisions as a function of collision energy. Empty symbols are for calculations with the SRP-MSINDO Hamiltonians to describe the CX_4 intramolecular potential and filled circles are for calculations with the AM1 Hamiltonian to describe the CF_4 intramolecular potential.

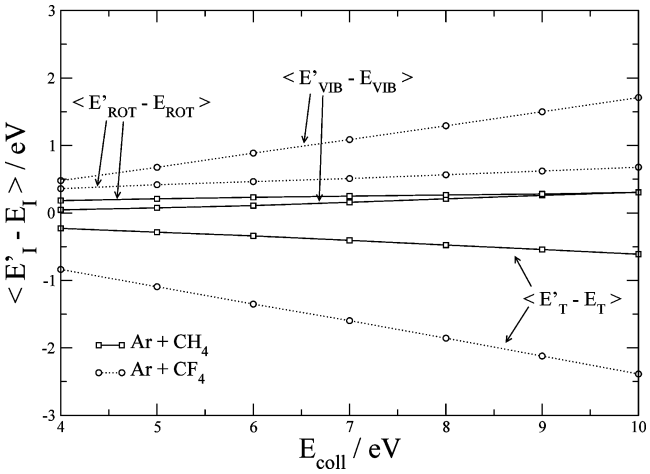

Figure 8. Average energy differences between reagents and products in Ar + CX_4 (X = H, F) collisions as a function of collision energy.

so that at E_{coll} = 10.0 eV, the average fractions in CH_4 rotation and vibration are roughly identical. On the other hand, most of the energy channeled into CF_4 goes into vibration at all energies, and the difference between the average fraction going to vibration and that into rotation increases with collision energy.

Figure 8 shows average changes in translational, rotational, and vibrational energy from reagents to products. Clearly, the amount of translational energy lost by the Ar atom increases with increasing collision energy in both Ar + CH_4 and Ar + CF_4 collisions. However, energy transfer to molecular modes is more efficient in Ar + CF_4, as noted before. The amount of vibrational energy gained by the alkane molecules during the collisions increases with collision energy, but the increase is larger in the case of CF_4. At E_{coll} = 10 eV, the average gain in vibrational energy by CF_4 is 5.6 times larger than that in CH_4. Regarding rotational gain, Figure 8 shows that the average increase in rotational energy is essentially independent of collision energy in CH_4, and it increases very moderately in CF_4. At E_{coll} = 10 eV the amount of rotational energy gained by CF_4 is 2.2 larger than that by CH_4. Although the moments of inertia around the principal axes of the CF_4 molecule are ∼27 times larger than those in CH_4, we see that the amount of energy transferred to rotation is only slightly larger in Ar + CF_4 collisions. This suggests that the values of the moments of

TABLE 4: Average Product Energies in Ar + CX_4 (X = H, F) Collisions for Different Combinations of Masses and Potential Energy Surfaces (PES) at E_{coll} = 10 eV

intramolecular PES	intermolecular PES	mass of X[a]	$\langle E'_T \rangle$/eV	$\langle E'_{INT} \rangle$/eV
Ar + CH_4				
CH_4	Ar−CH_4	H	9.28	0.72
CH_4	Ar−CH_4	F	8.73	1.27
CH_4	Ar−CF_4	F	7.95	2.05
Ar + CF_4				
CF_4	Ar−CF_4	F	7.61	2.39
CF_4	Ar−CF_4	H	8.63	1.37
CF_4	Ar−CH_4	H	9.03	0.97

[a] Mass of the X atom in the CX_4 molecules used to generate the initial conditions and propagate the trajectories.

inertia (and therefore the mass) are not closely connected with T → ROT′ energy transfer at hyperthermal energies. This result has been reported before in trajectory calculations of energy transfer from hot hydrogenated and perfluorinated benzene molecules to thermal noble gases.[38]

What we learn from these studies of collisional energy transfer is that T → VIB′, ROT′ energy transfer is much more efficient in hyperthermal Ar + CF_4 collisions than in Ar + CH_4 collisions. The differences between the results of the hydrogenated and fluorinated alkanes increase with collision energy. The enhancement of collisional energy transfer with fluorination has been observed before in studies of VIB → T′ energy transfer. Both experiments[39−41] and calculations[38] have shown that deactivation of highly excited perfluorobenzene molecules through collisions with thermal noble gases is much more effective than deactivation of benzene molecules. The calculations showed that the larger energy transfer in fluoroalkanes is mainly due to the change in mass, which decreases the vibrational frequencies. Geometry and potential energy surface effects appeared to be minor in comparison with the effect of the mass change.

To shed light on the factors controlling the differences in energy transfer in hyperthermal Ar + CX_4 (X = H, F) collisions, we have carried out additional calculations in which we vary both the mass of the X atom and the intermolecular potential energy surface. First, we have simulated Ar + CH_4 collisions at E_{coll} = 10 eV in which each H atom has the mass of a F atom. The trajectories are integrated by using the $ArCH_4$ global potential energy surface. Analogously, we have performed a calculation of Ar + CF_4 collisions at E_{coll} = 10 eV in which the mass of the F atoms is reduced to that of H atoms, but using the $ArCF_4$ potential energy surface. Table 4 shows the average energies in products' translation and vibration for these sets of calculations compared with the original results. The results of the table indicate that the change in mass accounts for a large fraction of the reported differences in the dynamics of Ar + CX_4 collisions. Ar + CH_4 trajectories integrated with the $ArCH_4$ potential energy surface in which the mass of H is replaced by that of F remarkably enhance the amount of T → INT′ energy transfer. Conversely, if we integrate Ar + CF_4 trajectories with the $ArCF_4$ potential energy surface, but replacing the mass of F by that of H, we find that the T → INT′ energy transfer decreases. The increase in the alkane mass upon fluorination leads to a decrease in the fundamental vibrational frequencies. Therefore, as has been shown before,[38] we can conclude that the coupling between translational and vibrational motions leading to collisional energy transfer is more effective with smaller vibrational frequencies in the molecule receiving the energy.

Although the change in the mass explains the trends of energy transfer in hyperthermal Ar + CH_4 and Ar + CF_4 collisions, it does not account quantitatively for all of the differences. Other factors, such as the different shape of the potential energy surface, seem to be involved. To gain insight into potential energy surface effects on energy transfer, we have carried out additional calculations for Ar + CH_4 collisions in which we both change the mass of the H atoms by that of F atoms and use the Ar−CF_4 intermolecular potential energy surface instead of the Ar−CH_4 one (the intramolecular potential remains unchanged). Table 4 shows that changing the intermolecular potential in addition to changing the mass brings the amount of energy transfer in Ar + CH_4 collisions closer to what we get in the regular Ar + CF_4 collisions. Similarly, when we carry out Ar + CF_4 calculations replacing the mass of the F atoms by that of H atoms, and using the Ar−CH_4 intermolecular potential energy surface, we see that the amount of energy transfer becomes quite close to that in the regular Ar + CH_4 collisions. These results show that the topology of the intermolecular potential energy surface is also involved in energy transfer at hyperthermal energies. The repulsive wall of the intermolecular potential is steeper in Ar−CF_4 than in Ar−CH_4. For instance, the slope of the curves in Figure 1a,b for the collinear approach at energies of about 8 eV is 29.4 eV/Å in Ar−CF_4 and 26.4 eV/Å in Ar−CH_4. Steeper repulsive walls have been seen to induce larger energy transfer before,[13] and this is what we see in Ar + CH_4 and Ar + CF_4 collisions at hyperthermal energies.

C. Comparison with Ar + C_2H_6. In a recent paper, Brunsvold et al. reported experimental and calculated product translational energy distributions in inelastic scattering of hyperthermal Ar from C_2H_6.[13] The availability of these data provides an opportunity to examine the effect of the hydrocarbon length on energy transfer. Direct comparison between the previously calculated data on Ar + C_2H_6 and the present work on Ar + CH_4 cannot be made for a variety of reasons. The intermolecular and intramolecular potentials in both studies are different. In the Ar + C_2H_6 work, Brunsvold et al. used the Ar−CH_4−III intermolecular potential of Hase and co-workers[18] and the original MSINDO Hamiltonian to describe the C_2H_6 potential. In this work, we use a newly developed intermolecular potential and a SRP-MSINDO Hamiltonian. In addition, the present calculations consider the flux scattered in the 180−5° angular interval, whereas the previous analysis was restricted to Ar atoms scattered in the backward hemisphere (180−90° angular interval).

To establish fair comparisons between energy transfer in Ar + C_2H_6 and Ar + CH_4 collisions, we have performed new calculations for both systems. We use the pairwise intermolecular potential developed in this work to describe the Ar + hydrocarbon interactions, and the original MSINDO Hamiltonian to describe the hydrocarbon intramolecular potential. Using this potential energy surface, we have calculated 5000 trajectories for both systems at E_{coll} = 5 eV, and our analysis is restricted to the 180−90° angular interval to emphasize collisions in which there is a hard hit between the noble gas and the hydrocarbon, leading to enhanced energy transfer.

The average product energies in Ar + CH_4 under such conditions are E'_T =4.49 eV, E'_{VIB} = 0.15 eV, and E'_{ROT}= 0.36 eV. The corresponding average product energies in Ar + C_2H_6 collisions are E'_T =3.84 eV, E'_{VIB} = 0.42 eV, and E'_{ROT}= 0.74 eV. These data reveal that increasing the length of the hydrocarbon leads to an increase in the efficiency of energy transfer. We attribute the reason for this behavior to the presence

of a larger number of low-frequency vibrational modes in ethane, which facilitates energy transfer from relative translation to molecular modes.

Comparison of the Ar + CH_4 results calculated with the original MSINDO Hamiltonian with the results calculated with the SRP-MSINDO data provides information about the effect of the intramolecular potential on energy transfer. We find that the average product energies with the SRP-MSINDO Hamiltonian ($E'_T = 4.46$ eV, $E'_{VIB} = 0.24$ eV, and $E'_{ROT} = 0.30$ eV) overlap with those produced with the original MSINDO Hamiltonian ($E'_T = 4.49$ eV, $E'_{VIB} = 0.15$ eV, and $E'_{ROT} = 0.36$ eV). (Both sets of average energies have been generated considering the trajectories scattered in the 180−90° angular interval.) Thus, we can conclude that the differences between the SRP-MSINDO and MSINDO Hamiltonians that describe the CH_4 intramolecular potential do not produce appreciable differences in Ar + CH_4 energy transfer at $E_{coll} = 5$ eV.

To delve further into the effect of the intramolecular potential on energy transfer, we have interfaced our trajectory propagator with the GAMESS suite of programs and performed Ar + CF_4 calculations using the AM1 Hamiltonian to describe the CF_4 potential. In these calculations, we use the same intermolecular potential of the previous calculations with the SRP-MSINDO Hamiltonian. We have calculated 5000 trajectories at $E_{coll} = 5$ and 10 eV, using the initial-conditions generation scheme described above for the SRP-MSINDO calculations. The results are shown in Figure 7, where one can see that the average fractions of product energies calculated with the AM1 Hamiltonian overlap with those calculated with the SRP-MSINDO Hamiltonian at $E_{coll} = 5$ and 10 eV. This result suggests that the intramolecular potential energy surface is not as important as the intermolecular potential energy surface in the calculation of average energy transfer in Ar + CF_4 collisions at hyperthermal energies.

D. Collision-Induced Dissociation. The substantial T → INT′ energy transfer seen in Ar + CX_4 collisions, particularly for X = F, together with the large collision energies considered in this study suggest that there might be collisions in which the amount of energy transferred to the CX_4 molecule is larger than needed to break a C−X bond. In this section, we investigate collision-induced dissociation in CX_4 molecules upon collisions with hyperthermal Ar atoms.

Collision-induced dissociation in Ar + CX_4 collisions can occur via two mechanisms. First, a bond in the alkane can break while the hyperthermal projectile is interacting with the alkane. We term this mechanism "prompt" collision-induced dissociation. A second possibility is that the energy transferred from relative translation to the internal modes of the molecule is above the dissociation energy of a C−H or C−F bond, but no dissociation occurs before Ar is completely removed from the molecule. The fate of these highly excited alkanes is 2-fold. The molecules can dissociate unimolecularly after some time, or can enter periodic internal motion that prevents dissociation.

Our calculations reveal that prompt collision-induced dissociation is rare, and most of the trajectories that receive energy above the dissociation asymptote do not dissociate in a time scale of a few hundred femtoseconds after the inner turning point of the trajectories. Specifically, we have detected only three trajectories producing CF_3 + F while Ar is still within interaction distance at $E_{coll} = 10$ eV (∼200 fs after the inner turning point of the trajectory). Figure 9 shows representative snapshots of one of these trajectories to illustrate the microscopic reaction mechanisms whereby prompt collision-induced dissociation occurs. In the collision, the Ar atom approaches with a small impact parameter (0.60 Å) roughly along one of the F−C−F bisectors. The F−C−F angle opens as the Ar atom reaches the inner turning point, resulting in dissociation of the C−F bond closest to the Ar atom impact. No CH_4 molecules are seen to decay to CH_3 + H in a 200 fs time scale even at $E_{coll} = 10$ eV.

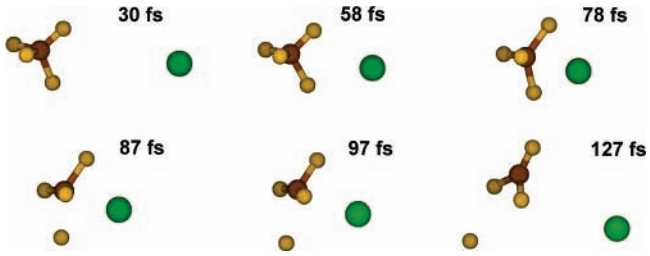

Figure 9. Selected snapshots of an Ar + CF_4 trajectory giving rise to prompt collision-induced dissociation. $E_{coll} = 10$ eV.

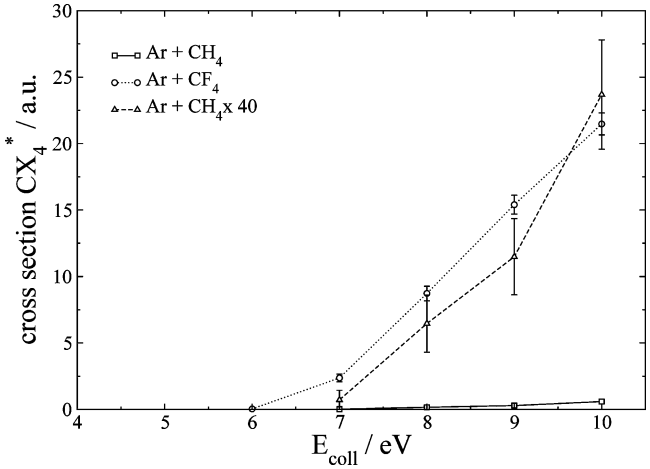

Figure 10. Cross sections of Ar + CX_4 (X = H, F) collisions generating CX_4 molecules with internal energy above the C−X dissociation energy limit as a function of collision energy. The dissociation energy for the C−H bond is 4.802 eV, and that for the C−F bond is 5.736 eV (see Table 2). The dashed line connecting triangles represents the cross sections for Ar + CH_4 trajectories multiplied by a factor of 40.

Unfortunately, the computational expense of our direct-dynamics approach does not allow us to integrate the trajectories for long enough to distinguish whether CX_4 molecules receiving energy in excess of the C−X bond dissociation energy undergo a unimolecular dissociation process or not. Under experimental conditions, highly excited molecules can live for as long as a few microseconds before they decay due to collisional processes with ambient species or arrive at the detector. Delayed collision-induced dissociation can occur anywhere in that time scale. Although our theoretical approach prohibits us from following trajectories for such a long time, a rough estimate of the different extent of collision-induced dissociation between hydrogenated and fluorinated alkanes can be given by comparing the cross sections of trajectories in which the CX_4 molecules receive excitation above the dissociation limit. We note that this cross section does not correspond to a collision-induced dissociation cross section, and only represents an upper limit to it.

Figure 10 shows the cross sections of trajectories in which the amount of T → INT′ energy transfer exceeds the C−X (X = H, F) dissociation limit (according to SRP-MSINDO calculations) in the corresponding CX_4 molecules. The figure demonstrates that the amount of trajectories in which the CX_4 molecule receives excitation above the dissociation limit is larger for fluorinated alkanes than for hydrogenated collisions. On the

basis of these results, we tentatively suggest that the absolute cross sections of collision-induced dissociation in fluorinated alkanes are much larger than those in hydrogenated alkanes.

Noticeably, although the C−X bond is roughly 1 eV stronger in CF_4 than in CH_4, Figure 10 shows that the threshold for excitation of the CX_4 molecule above the dissociation limit is 1 eV smaller for Ar + CF_4 than for Ar + CH_4 (threshold ∼6 eV for Ar + CF_4 and 7 eV for Ar + CH_4). At collision energies above the threshold, the cross section for CX_4 with energy above the C−X dissociation limit is approximately 40 times larger for CF_4 than for CH_4. The large sizes of the cross sections in Figure 10 are a consequence of the high probability for transferring large amounts of energy in Ar + CX_4 collisions, and the large impact parameter at which this can happen. For instance, at $E_{coll} = 10$ eV, CF_4 results with internal excitation above the CF_3−F limit in 598 trajectories out of 5000 trajectories started with a quadratic distribution of impact parameters between 0 and 4 Å (7.56 au).

The cross sections in Figure 10 refer to trajectories in which CX_4 possesses *internal* (i.e., vibrational + rotational) energy above the asymptote. It might be argued that a more accurate procedure to estimate the upper limit of collision-induced dissociation cross sections would be to consider trajectories in which CX_4 arises with *vibrational* energy above the CX_3 + X asymptote. With use of this procedure, the cross section for Ar + CH_4 trajectories generating CH_4 with vibrational energy larger than 4.802 eV (C−H dissociation energy in SRP-MSINDO) is 0.09 ± 0.04 au, while that for Ar + CF_4 trajectories producing CF_4 with vibrational energy above the CF_3 + F limit (5.736 eV according to SRP-MSINDO) is 6.93 ± 0.49 au. Although this procedure has limited use due to the expected coupling of rotational and vibrational modes, we see that regardless of the algorithm used to define the amount of excitation in the CX_4 product, hyperthermal Ar + CF_4 collisions are more than 1 order of magnitude more likely to produce excitation above the C−X dissociation asymptote than Ar + CH_4 collisions.

Calculations of Ar + CF_4 collisions with the AM1 Hamiltonian at 10 eV point out the deficiencies of this potential-energy method for collision-induced dissociation. In effect, we have observed 12 trajectories that lead to prompt collision-induced dissociation, a 4-fold increase over the predictions of the SRP-MSINDO Hamiltonian using analogous initial conditions. The reason for this sharp increase of collision-induced dissociation is that the AM1 Hamiltonian underestimates the C−F dissociation energy by more than 1 eV (see Table 2). As we have seen before, AM1 quantitatively reproduces the *average* fractions of product energy predicted by the SRP-MSINDO potential. However, the extent of collision-induced dissociation is not well reproduced by AM1. Thus, what we learn from this study is that although one can use intramolecular potentials with an incorrect dissociation limit to describe average energy transfer, calculations of events in which a large amount of energy transfer leads to collision-induced dissociation require accurate potentials.

Concluding Remarks

We have investigated energy transfer and collision-induced dissociation in collisions between hyperthermal Ar and the CH_4 and CF_4 molecules using the quasiclassical trajectory method. The inter- and intramolecular potential energy terms are built based on high-quality ab initio calculations for both systems. While the Ar−CX_4 (X = H, F) intermolecular potential energy surface is represented by generalized exponential functions, the CX_4 intramolecular potential energy surface presents a challenge due to the possibility of bond-breakage during the collision. We describe a practical approach to develop intramolecular potential energy surfaces for dissociating molecules based on improving semiempirical Hamiltonians with grids of ab initio data. The semiempirical Hamiltonians improved in this way can provide accurate estimates of the intramolecular potential energy throughout a wide range of energies and molecular configurations. The specific-reaction-parameters semiempirical Hamiltonians have very competitive computation times and can be used directly to propagate thousands of trajectories for systems such as the ones studied here.

Direct-dynamics studies of Ar + CH_4 and Ar + CF_4 collisions enable us to learn that fluorination dramatically increases the amount of collisional energy transfer from initial translation to molecular modes. While the efficiency of fluorination had been previously reported in studies of VIB → T′ energy transfer from highly vibrationally excited molecules to noble-gas baths, the large enhancement in T → VIB′ energy transfer due to fluorination is a novel result in hyperthermal collisions of noble gases with thermal molecules. We show that the different extent of energy transfer in hydrogenated and fluorinated alkanes stems from mainly the difference in mass and the shape of the intermolecular potential energy surface. Fluorination decreases the value of the vibrational frequencies of the CX_4 molecule and increases the steepness of the intermolecular potential energy surface. Both of these effects result in enhanced energy transfer.

The enhanced energy transfer upon fluorination leads to large cross sections for excitation of CF_4 molecules above the CF_3−F dissociation energy limit. In addition, while we observe prompt collision-induced dissociation for Ar + CF_4 collisions at $E_{coll} = 10$ eV, we do not detect that channel in Ar + CH_4.

Analysis of the effect of the intramolecular potential energy surface reveals that the average fractions of product energies are not very sensitive to the intramolecular surface under the initial conditions explored in our calculations. However, strong underestimations of the CF_3−F dissociation energy lead to strong overestimations of collision-induced dissociation.

The findings reported in this paper open new lines of thought in our understanding of how materials degrade in low-Earth orbit. While many studies show that regular (hydrogenated) polymeric hydrocarbons erode under the action of hyperthermal atomic oxygen at 5 eV,[7] recent studies show that the reactivity of fluorinated hydrocarbons with hyperthermal atomic oxygen is marginal.[15] Although fluorinated polymers (such as TEFLON) show better resistance to LEO environment than hydrogenated polymers, they still degrade in low-Earth orbit.[14] Since the reactivity of atomic oxygen alone does not explain the reduced but appreciable degradation of fluorinated polymers, other erosion causes need to be characterized. Our work suggests that fluorination enhances the collision-induced dissociation pathway for erosion arising from impacts with hyperthermal-energy heavy closed-shell species such as N_2 and Ar.

Future work will address the effect of fluorination in collision-induced dissociation of longer-chain gas-phase alkanes and condensed surfaces, using the technology described here to generate multidimensional potential energy surfaces. The dynamics of gas/surface and gas-phase collisions are rather different, inhibiting an accurate estimation of the gas/surface behavior from gas-phase data. A surface provides a pool of low-frequency, large-amplitude modes that are not present in small gas-phase molecules. These modes will, in principle, help dissipate the energy from the impact point toward the surface, averting collision-induced dissociation. However, if the energy dissipation toward the surface is not fast, and energy is initially

transferred to local molecular modes in the surface, collision-induced dissociation will likely take place.

Acknowledgment. This work has been supported by a new faculty start-up allowance from the Department of Chemistry at Virginia Tech. T. Daniel Crawford and John R. Morris (Chemistry Department, Virginia Tech) are also acknowledged for their insightful comments and permanent encouragement.

References and Notes

(1) Hippler, H.; Troe, J. In *Bimolecular Collisions*; Baggot, J. E., Ashfold, M. N. R., Eds.; The Royal Society of Chemistry: London, UK, 1989; p 209.

(2) Oref, I.; Tardy, D. C. *Chem. Rev.* **1990**, *90*, 1407.

(3) Lendvay, G.; Schatz, G. C. In *Advances in Chemical Kinetics and Dynamics*: *Vibrational Energy* Transfer *Involving Large and Small Molecules*; Barker, J. R., Ed.; JAI Press: Greenwich, CT, 1995; Vol. 2B, p 245.

(4) Mullin, A. S.; Schatz, G. C. *Dynamics of highly excited states in chemistry*: *an overview*; ACS Symp. Ser. No. 678, Highly Excited Molecules; American Chemical Society: Washington, DC, 1997.

(5) Leger, L. J.; Visentine, J. T. *J. Spacecr. Rockets* **1986**, *23*, 505.

(6) Murr, L. E.; Kinard, W. H. *Am. Sci.* **1993**, *81*, 152.

(7) Minton, T. K.; Garton, D. J. Dynamics of Atomic-Oxygen-Induced Polymer Degradation in Low Earth Orbit. In *Advances Series in Physical Chemistry*; Vol. 11, Chemical Dynamics in Extreme Environments; Dressler, R. A., Ed.; World Scientific: Singapore, 2001; p 420.

(8) Garton, D. J.; Minton, T. K.; Troya, D.; Pascual, R.; Schatz, G. C. *J. Phys. Chem. A* **2003**, *107*, 4583.

(9) Troya, D.; Schatz, G. C. *Int. Rev. Phys. Chem.* **2004**, *23*, 341.

(10) Troya, D.; Schatz, G. C. Dynamics studies of the O(3P)+CH_4, C_2H_6 and C_3H_8 reactions. In *Theory of Chemical Reaction Dynamics*; Lagana, A., Lendvay, G., Eds.; Kluwer Academic Publishers: Dordrecht, The Netherlands, 2004; p 329.

(11) Minton, T. K.; Zhang, J.; Garton, D. J.; Seale, J. W. *High Performance Polymers* **2000**, *12*, 27.

(12) Zhang, J.; Minton, T. K. *High Perform. Polym.* **2001**, *13*, S467.

(13) Brunsvold, A. L.; Garton, D. J.; Minton, T. K.; Troya, D.; Schatz, G. C. *J. Chem. Phys.* **2004**, *121*, 11702.

(14) Koontz, S. L.; Leger, L. J.; Visentine, J. T.; Hunton, D. E.; Cross, J. B.; Hakes, C. L. *J. Spacecr. Rockets* **1995**, *32*, 483.

(15) Troya, D.; Schatz, G. C. *Theoretical Study of Reactions of Hyperthermal O(3P) with Perfluorinated Hydrocarbons*; Proceedings of the 7th International Conference on Protection of Materials and Structures from Space Environment, Toronto, 2005.

(16) Rasoul, F. A.; Hill, D. J. T.; George, G. A.; O'donnell, J. H. *Polym. Adv. Technol.* **1998**, *9*, 24.

(17) Chen, J. X.; Tracy, D.; Zheng, S.; Xiaolu, L.; Brown, S.; VanDerveer, W.; Entenberg, A.; Vukanovic, V.; Takacs, G. A.; Egitto, F. D.; Matienzo, L. J.; Emmi, F. *Polym. Degrad. Stab.* **2003**, *79*, 399.

(18) Sun, L.; de Sainte Claire, P.; Meroueh, O.; Hase, W. L. *J. Chem. Phys.* **2001**, *114*, 535.

(19) Duchovic, R. J.; Hase, W. L.; Schlegel, H. B.; Frisch, M. J.; Raghavachari, K. *Chem. Phys. Lett.* **1982**, *89*, 120.

(20) Duchovic, R. J.; Hase, W. L.; Schlegel, H. B. *J. Phys. Chem.* **1984**, *88*, 1339.

(21) Duchovic, R. J.; Hase, W. L. *Chem. Phys. Lett.* **1984**, *110*, 474.

(22) Hase, W. L.; Date, N.; Bhuiyan, L. B.; Buckowski, D. G. *J. Phys. Chem.* **1985**, *89*, 2502.

(23) Hu, X.; Hase, W. L. *J. Phys. Chem.* **1988**, *92*, 4040.

(24) Bolton, K.; Hase, W. L. Direct dynamics simulations of reactive systems. In *Modern Methods for Multidimensional Dynamics Computations in Chemistry*; Thompson, D. L., Ed.; World Scientific: Singapore, 1998; p 143.

(25) Bredow, T.; Jug, K. *Theor. Chem. Acc.* **2005**, *113*, 1.

(26) Dutta, A.; Sherrill, C. D. *J. Chem. Phys.* **2003**, *118*, 1610.

(27) Ahlswede, B.; Jug, K. *J. Comput. Chem.* **1999**, *20*, 572.

(28) Jug, K.; Geudtner, G.; Homann, T. *J. Comput. Chem.* **2000**, *21*, 974.

(29) Dewar, M. J. S. Z.; Eve G.; Healy, E. F.; Stewart, J. J. P. *J. Am. Chem. Soc.* **1985**, *107*, 3902.

(30) Stewart, J. J. P. *J. Comput. Chem.* **1989**, *10*, 209.

(31) Frisch, M. J.; Trucks, G. W.; Schlegel, H. B.; Scuseria, G. E.; Robb, M. A.; Cheeseman, J. R.; Montgomery, J. A., Jr.; Vreven, T.; Kudin, K. N.; Burant, J. C.; Millam, J. M.; Iyengar, S. S.; Tomasi, J.; Barone, V.; Mennucci, B.; Cossi, M.; Scalmani, G.; Rega, N.; Petersson, G. A.; Nakatsuji, H.; Hada, M.; Ehara, M.; Toyota, K.; Fukuda, R.; Hasegawa, J.; Ishida, M.; Nakajima, T.; Honda, Y.; Kitao, O.; Nakai, H.; Klene, M.; Li, X.; Knox, J. E.; Hratchian, H. P.; Cross, J. B.; Bakken, V.; Adamo, C.; Jaramillo, J.; Gomperts, R.; Stratmann, R. E.; Yazyev, O.; Austin, A. J.; Cammi, R.; Pomelli, C.; Ochterski, J. W.; Ayala, P. Y.; Morokuma, K.; Voth, G. A.; Salvador, P.; Dannenberg, J. J.; Zakrzewski, V. G.; Dapprich, S.; Daniels, A. D.; Strain, M. C.; Farkas, O.; Malick, D. K.; Rabuck, A. D.; Raghavachari, K.; Foresman, J. B.; Ortiz, J. V.; Cui, Q.; Baboul, A. G.; Clifford, S.; Cioslowski, J.; Stefanov, B. B.; Liu, G.; Liashenko, A.; Piskorz, P.; Komaromi, I.; Martin, R. L.; Fox, D. J.; Keith, T.; Al-Laham, M. A.; Peng, C. Y.; Nanayakkara, A.; Challacombe, M.; Gill, P. M. W.; Johnson, B.; Chen, W.; Wong, M. W.; Gonzalez, C.; Pople, J. A. *Gaussian 03*, Revision C.02; Gaussian Inc.: Wallingford, CT, 2004.

(32) Schmidt, M. W.; Baldridge, K. K.; Boatz, J. A.; Elbert, S. T.; Gordon, M. S.; Jensen, J. H.; Koseki, S.; Matsunaga, N.; Nguyen, K. A.; Su, S. J.; Windus, T. L.; Dupuis, M.; Montgomery, J. A. *J. Comput. Chem.* **1993**, *20*, 1347.

(33) Yan, T.; Doubleday: C.; Hase, W. L. *J. Phys. Chem. A* **2004**, *108*, 9863.

(34) Troya, D.; Garcia-Molina, E. *J. Phys. Chem. A* **2005**, *109*, 3015.

(35) Gonzalez-Lafont, A.; Truong, T. N.; Truhlar, D. G. *J. Phys. Chem.* **1991**, *95*, 4618.

(36) http://www.netlibg.org.

(37) Hase, W. L.; Duchovic, R. J.; Hu, X.; Komornicki, A.; Lim, K. F.; Lu, D.-H.; Peslherbe, G. H.; Swamy, K. N.; vande Linde, S. R.; Varandas, A. J. C.; Wang, H.; Wolf, R. J. *VENUS96*, A general chemical dynamics computer program, 1996.

(38) Lenzer, T.; Luther, K.; Troe, J.; Gilbert, R. G.; Lim, K. F. *J. Chem. Phys.* **1995**, *103*, 626.

(39) Toselli, B. M.; Barker, J. R. *J. Chem. Phys.* **1992**, *97*, 1809.

(40) Yerram, M. L.; Brenner, J. D.; King, K. D.; Barker, J. R. *J. Phys. Chem.* **1990**, *94*, 6341.

(41) Damm, M.; Hippler, H.; Olschewski, H. A.; Troe, J.; Willner, J. *Z. Phys. Chem.* **1990**, *166*, 129.

(42) NIST Computational Chemistry Comparison and Benchmark Database. http://srdata.nist.gov/cccbdb. IV. A.1 Reaction Comparison. Experimental Enthalpies at 0 K.

(43) Chase, M. W., Jr.; Davies, C. A.; Downey, J. R., Jr.; Frurip, D. J.; McDonald, R. A.; Syverud, A. N. *J. Phys. Chem. Ref. Data* **1985**, *14*, *Suppl. 1*, 595.

(44) Baulch, D. L.; Cox, R. A.; Hampson, R. F.; Kerr, J. A.; Troe, J.; Watson, R. T. *J. Phys. Chem. Ref. Data* **1980**, *9*, 467.

(45) Simanouchi, T. *Tables of Molecular Vibrational Frequencies Consolidated*; National Bureau of Standards: Washington, DC, 1972; Vol. I, p 1.

(46) Forney, D.; Jacox, M. E.; Irikura, K. K. *J. Chem. Phys.* **1994**, *101*, 8290.